



Effects of Zn^{2+} substitution on the structural, morphological, DC electrical resistivity, permeability and magnetic properties of $\text{Co}_{0.5}\text{Cu}_{0.5-x}\text{Zn}_x\text{Fe}_2\text{O}_4$ nanoferrite

Hanumantha Rao Daruvuri¹ · N. Murali² · M. Madhu³ · A. Ramakrishna^{4,5} · D. Parajuli⁶ · M. P. Dasari¹

Received: 25 February 2022 / Accepted: 29 November 2022 / Published online: 28 December 2022

© The Author(s), under exclusive licence to Springer-Verlag GmbH, DE part of Springer Nature 2022, corrected publication 2023

Abstract

A strong magnet of $\text{Co}_{0.5}\text{Cu}_{0.5-x}\text{Zn}_x\text{Fe}_2\text{O}_4$ ($x = 0.0, 0.1, 0.2, 0.3, 0.4$ and 0.5) was prepared by using the sol–gel auto-combustion technique. Using XRD, FESEM, HRTEM, FTIR, and VSM, the synthesized samples' structural and functional group, and permeability, magnetic and DC electrical resistivity properties were studied. The structure was found to be cubic spinel. The average crystallite sizes were found to be 40–60 nm. With an increase in Zn^{2+} ion replacement, the lattice constant increases. Field effect scanning electron microscopy (FESEM) and HRTEM are both used to examine the surface morphology and crystalline nature. Two absorption bands around 600 and 400 cm^{-1} related to tetrahedral (A) and octahedral (B) interstitial sites by FTIR agree with the spinel lattice. All possible parameters are responsible for enhancing the magnetic quality identified and presented in this work. These are highly suitable for multi-layer ferrite chip inductor applications with a considerable enhancement in permeability. Magnetic properties have been explained on the basis of cation distribution. The sample's hysteresis curves showed that the saturation magnetization and coercivity decreased after Zn^{2+} ions were replaced in the Co–Cu nanoferrites. The ferrite samples were semiconducting because the DC electrical resistivity decreased as temperature increased.

Keywords Co–Zn ferrite · XRD · Spinal structure · FTIR · Permeability · VSM

1 Introduction

The exotic properties of ferrite NPs applied in advanced fields, such as magnetic recording media, wave absorbers, and microwave devices, have attracted their thorough studies in recent years using different synthesis methods [1–3]. They have a spinel structure with an AB_2O_4 form [4]. Cobalt ferrite CoFe_2O_4 is a hard ferrite with a partially inverted spinel structure due to the prevalence of cobalt atoms in the octahedral sites [5]. The magnetic moment of Fe^{3+} ions is $M = 5\mu\text{B}$ and it occupies the tetragonal A sites, while the B site contains Co^{2+} ions ($M = 3\mu\text{B}$) and Fe^{3+} ions [6]. The addition of metal cations with different valence states results in different distributions of A and B sites in the ferrites [7]. The cation distribution in the two interstitial sites of the spinel cubic structure affects its properties [8], especially in the physical properties [9]. In addition, the partial Cu^{2+} substitution affects the structure [10] that is suitable for sensors and actuator-like devices through improved electrical resistivity [11]. Ferrites can be synthesized [12] by several processes such as microemulsion, ceramic, co-precipitation, hydrothermal, and sol–gel auto-combustion

✉ N. Murali
muraliphdau@gmail.com

✉ M. P. Dasari
madhavaprasaddasari@gmail.com

¹ Department of Physics, GIS, GITAM (Deemed to Be University), Visakhapatnam 530045, Andhra Pradesh, India

² Department of Engineering Physics, AUCE (A), Andhra University, Visakhapatnam, India

³ Department of Physics, Anurag University, Hyderabad, Telangana 500088, India

⁴ Department of ECE, Aditya College of Engineering & Technology, Surampalem, India

⁵ Jawaharlal Nehru Technological University Kakinada, Kakinada, India

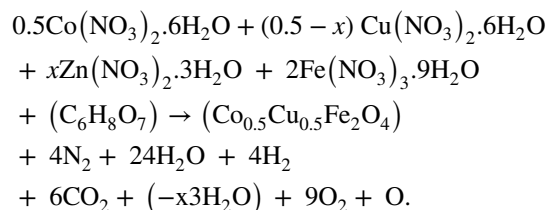
⁶ Research Center for Applied Science and Technology, Tribhuvan University, Kirtipur, Nepal

methods [13–15]. Because of its simplicity, good stoichiometric control, inexpensive precursors, ultrafine particles, brief processing time at very low temperatures, and other material properties, the sol–gel process was chosen in this work [16].

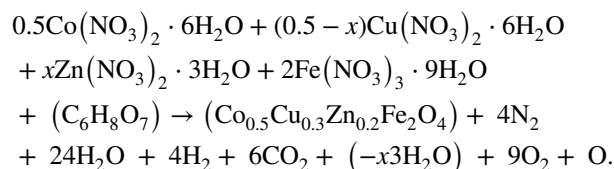
Studying the effects of Zn^{2+} substitution on the structural, microstructural magnetic, permeability, and DC electrical resistivity properties of Co–Cu ferrite $Co_{0.5}Cu_{0.5-x}Zn_xFe_2O_4$ is the aim of the present work (0.0, 0.1, 0.2, 0.3, 0.4 and 0.5).

2 Experimental techniques

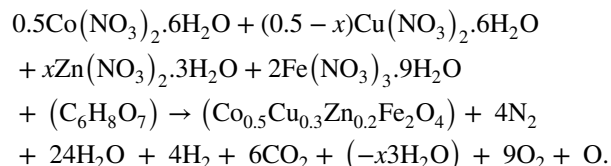
By using the sol–gel auto-combustion approach, $Co_{0.5}Cu_{0.5-x}Zn_xFe_2O_4$ ferrites ($x=0.0$ to 0.5 in increments of 0.1) were created. The cobalt, zinc, copper, and iron nitrates were added with citric acid (as a chelating agent) in a 1:1 ratio. In our earlier communication, we reported the synthesis process's details [17]. For additional characterizations, the as-obtained powders were formed into pellets and sintered for 3 h at $1000^\circ C$. Pellets of approximately 15 mm diameter were obtained by pressing the sintered powder of different compositions in a pellet-making die. Applying a hydraulic press, a load of 5 tons was employed for about 5 min. At $x=0$,



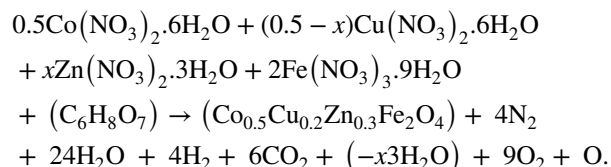
At $x=0.1$,



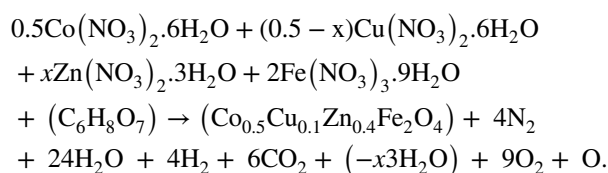
At $x=0.2$,



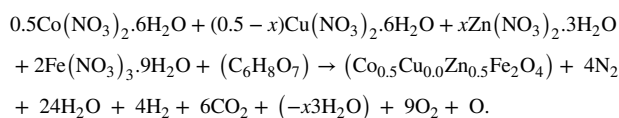
At $x=0.3$,



At $x=0.4$,



At $x=0.5$,



The Rigaku X-ray diffractometer (Rigaku Miniflex II) was used to analyze the structural characteristics of the materials. A TESCAN, MIRA II LMH-FESEM Inca Oxford was used for the morphological and compositional study. A JEOL 3010 with a UHR pole piece working at an accelerating voltage of 300 kV was used as a high-resolution transmission electron microscope (HRTEM). The EZ-VSM was used at room temperature for the magnetic function, FTIR for the functional group, and a two-probe system for DC resistivity, respectively, of the system. The permeability studies' specimens were measured by using Hewlett Packard Impedance Analyzer model 4192A. Complex permeability was calculated as a frequency function up to 1 MHz at 298 K using a conventional technique to determine the circuit's complex impedance loaded with toroid-shaped ferrites samples.

3 Results and discussion

3.1 XRD analysis

For the cubic single phase of $Co_{0.5}Cu_{0.5-x}Zn_xFe_2O_4$ (0.0, 0.1, 0.2, 0.3, 0.4 and 0.5) samples, XRD measurements were taken using $Cu-K\alpha$ ($\lambda = 1.5406 \text{ \AA}$). Scanning was done for 1 s in the range of 10° – 80° (2θ), the scan step size was 0.033° and gave the diffraction peaks at the (111), (220), (311), (222), (400), (422), (511) and (440) planes, showing single-phase spinel lattice and matched JCPDS card no. 02-1045 [18]. The XRD pattern of $Co_{0.5}Cu_{0.5-x}Zn_xFe_2O_4$ exhibited broad diffraction in the range 10° – 80° , corresponding to the amorphous SiO_2 matrix and cubic spinel $CoFe_2O_4$ crystalline single phase (JCPDS card no. 02–1045) indexed to the (111), (220), (311), (222), (400), (422), (511), and (440) planes. It is intriguing to observe that as the concentration of Zn^{2+} increases, the broadness of the diffracted peaks narrows, indicating that Zn^{2+} influences crystallite size. For all of the sintered samples, XRD was unable to detect any additional secondary phases.

Table 1 Lattice parameters of the CoCuZn nanoferrite system

Compounds (x)	Lattice constant (Å)	Crystallite size (nm)	Cell volume (Å) ³	Bulk density g/cm ³	X-ray density g/cm ³	Porosity (%)	r _A (Å)	R _B (Å)
Co _{0.5} Cu _{0.5} Fe ₂ O ₄	8.384	30	589	4.34	4.65	6.7	1.901	2.731
Co _{0.5} Cu _{0.4} Zn _{0.1} Fe ₂ O ₄	8.387	34	592	4.32	4.61	6.3	1.905	2.729
Co _{0.5} Cu _{0.3} Zn _{0.2} Fe ₂ O ₄	8.391	36	594	4.30	4.52	4.9	1.908	2.727
Co _{0.5} Cu _{0.2} Zn _{0.3} Fe ₂ O ₄	8.398	39	596	4.29	4.41	2.7	1.911	2.726
Co _{0.5} Cu _{0.1} Zn _{0.4} Fe ₂ O ₄	8.404	42	598	4.25	4.35	2.3	1.918	2.724
Co _{0.5} Zn _{0.5} Fe ₂ O ₄	8.409	45	599	4.24	4.31	1.6	1.925	2.723

When Zn²⁺ replaces Cu²⁺ ions, the lattice parameter (Å) of the sample increases due to the larger ionic radii of Zn²⁺ (0.83 Å) ions than Cu²⁺ (0.78 Å) ions. The tetrahedral (r_A) and octahedral (r_B) sites are obtained with

$$r_A = [C_{ACu}r(\text{Cu}^{2+}) + C_{AFe}r(\text{Fe}^{3+})],$$

$$r_B = \frac{1}{2} [C_{BZn}r(\text{Zn}^{2+}) + C_{BCu}r(\text{Cu}^{2+}) + C_{BCo}r(\text{Co}^{2+}) + C_{BFe}r(\text{Fe}^{3+})],$$

Where C_{ACu} and C_{AFe} represent the concentration of Cu²⁺ and Fe³⁺ at A site; and C_{BZn}, C_{BCu}, C_{BCo}, and C_{BFe} represent the concentration of Zn²⁺, Cu²⁺, Co²⁺ and Fe³⁺ at B site. *r* also denotes the ionic radii of appropriate ions Cu²⁺ (*r* = 0.73 Å), Co²⁺ (*r* = 0.74 Å), Fe³⁺ (*r* = 0.64 Å) and Zn²⁺ (*r* = 0.83 Å). The obtained results of r_A and r_B, lattice constants, and unit cell volumes of all samples are listed in Table 1.

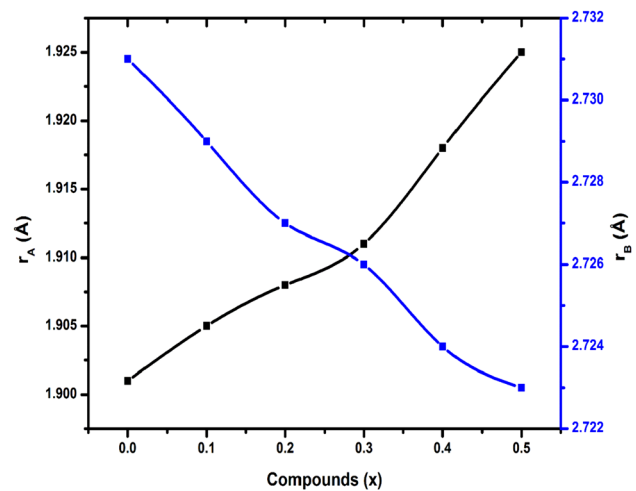
It is found that r_A is increased with increase of Zn²⁺ content from *x* = 0.1 to *x* = 0.5 in the synthesized samples. An increase in r_A with increasing Zn²⁺ content can be discussed based on the ionic radii of the cations involved in the tetrahedral sites. The ionic radius of the Zn²⁺ (0.83 Å) is greater than that of Fe³⁺ (0.64 Å) [19]. As seen in Fig. 1, some amount of the Fe³⁺ ions in the tetrahedral sites are replaced by Zn²⁺ ions, which causes the enlargement of the tetrahedral lattice, and hence r_A is increased. It also found that r_B is increased with Zn²⁺ content in the synthesized samples. Zn²⁺ ions with Cu²⁺ ions cause the transfer of some amounts of Fe³⁺ ions from A to B site. This may be considered as being responsible for shrinkages of the octahedral lattice, and hence r_B is decreased.

The lattice parameter is obtained by using the relation [20]:

$$a = d_{hkl} \sqrt{h^2 + k^2 + l^2},$$

where *d* is the interplanar spacing given by Bragg's law for the plane (hkl).

The diffraction peaks' observed broadness (Fig. 2) shows the samples' nanocrystalline structure. Observation of the XRD pattern reveals that broadening reduction is [21]

**Fig. 1** Variation of the tetrahedral (r_A) and octahedral (r_B) sites of CoCuZn nanoferrite system

$$D_{311} = \frac{0.9\lambda}{\beta \cos \theta},$$

where λ , β , and θ are, respectively, the X-ray wavelength (1.5406 Å), the full width at half maximum of the (311) peak, and the diffraction angle.

The variation of the lattice constant with the crystallite size of the CoCuZn nanoferrites system is shown in Fig. 3. With increasing Zn²⁺ concentration, there is a discernible progressive increase in crystallite size, which ranges from 30 to 45 nm.

The Archimedes principle gives the bulk density (*d_b*) of each sample, and its X-ray density (*d_x*) was calculated using a well-known relation [22].

$$d_x = \frac{ZM}{Na_0^3},$$

where *Z* = 8 is the number of molecules in one unit cell, *M* is the molecular weight of the particular ferrite, *N* is Avogadro's number, *a₀* is the experimental lattice constant, and *M* is its molecular weight.

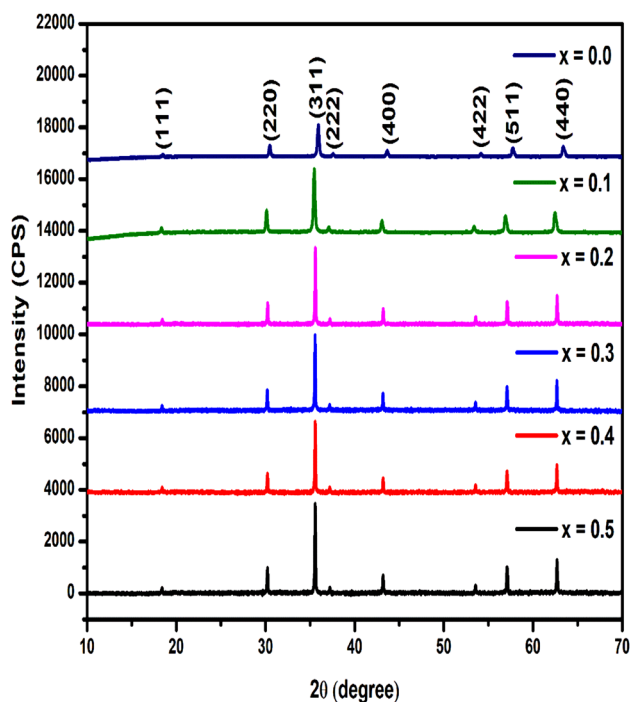


Fig. 2 XRD patterns of the CoCuZn nanoferrite system

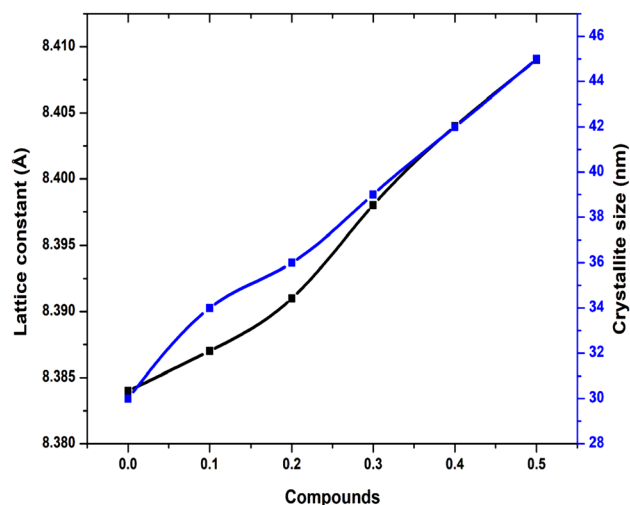


Fig. 3 Variation of lattice constant with the crystallite size of the CoCuZn nanoferrite system

Table 1 lists the variations in ' d_x ' and ' d_b ' values for CoCuZn nanoferrites. The bulk density, or $d_b < d_x$, is often lower than the X-ray density due to the formation of pores during sintering. It is evident that as Zn^{2+} concentration increases and ' d_x ' and ' d_b ' decrease. The decrease in the lattice constant decreases ' d_x '.

The porosity (p) [23] is

$$P = \left[\frac{d_x - d_b}{d_x} \right] \times 100.$$

The porosity variations for Co–Cu ferrites with Zn^{2+} substitutions were studied. As seen in Tab. 1, the difference between d_x and d_b becomes smaller with increasing Zn^{2+} , indicating decreasing porosities. The observation that Zn^{2+} addition to nickel ferrite leads to the densification of the material [24] is consistent with zinc ferrite having the least porosity.

Figure 4 shows the variation of the X-ray density (d_x), bulk density (d_b), and porosity (p) of the CoCuZn nanoferrite system and values are listed in Table 1.

The cation distribution in the interstitial sites affects the structural and magnetic properties of the ferrites [25]. Cu^{2+} and Zn^{2+} ions reside at A and B sites. Co^{3+} is found at both, and Fe^{3+} occupies the rest. The cation distributions in CoCuZn samples are shown in Table 2.

3.2 FESEM study

To determine the sample's shape, homogeneity, and grain size, scanning electron microscopy (SEM) is utilized. Figure 5 shows the FESEM images of $Co_{0.5}Cu_{0.5-x}Zn_xFe_2O_4$ ($x = 0.0, 0.1, 0.2, 0.3, 0.4$ and 0.5) nanoferrite where the Zn^{2+} substitution increases the grain size up to $x = 0.5$ and subsequently declines for higher x . It indicates that the material has crystallites that include spherical nanoparticles [26]. The distribution of the nanoparticles appears to be even and dense. A slight aggregation can be seen in the morphology. The particle sizes were found to be between 200 and 38 nm.

3.3 HRTEM study

The HRTEM images of the $Co_{0.5}Cu_{0.5-x}Zn_xFe_2O_4$ ($x = 0.0$ and 0.1) samples, including particle size of the bright field images, and selected area electron diffraction (SAED) of all the samples, are shown in Figs. 6a–c and 7a–b, respectively. These figures show the nanocrystalline nature of both pure and substituted nanoferrites. The particle size of the pure and substituted samples found agreed well with their XRD values. The SAED patterns show a clear diffraction pattern of pure and substituted crystalline nanoparticles [27]. The pattern can be assigned for the typical (hkl) values or planes of the synthesized samples.

From the selected area diffraction pattern (SAED), the corresponding planes were calculated using the relation [28]:

$$d = \frac{\lambda L}{R},$$

Fig. 4 Variation of X-ray density (dx), bulk density (db), and porosity (p) of the CoCuZn nanoferrite system

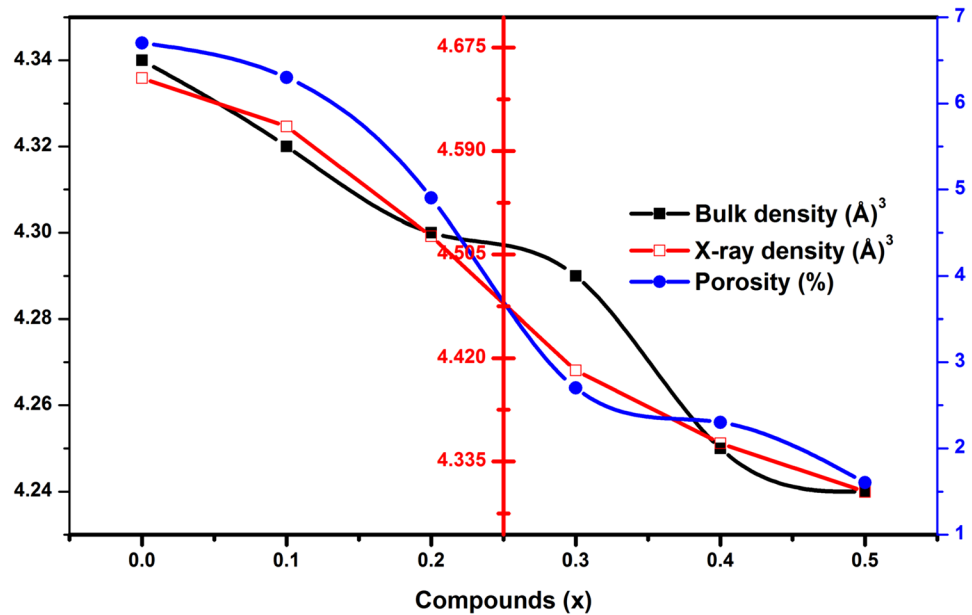


Table 2 Cation distribution in the Co_{0.5}Cu_{0.5-x}Zn_xFe₂O₄ samples

Cu content (x)	A site	B Site
Co _{0.5} Cu _{0.5} Fe ₂ O ₄	Co ²⁺ _{0.5} Fe ³⁺ _{0.5}	Co ²⁺ _{0.5} Fe ³⁺ _{1.5}
Co _{0.5} Cu _{0.4} Zn _{0.1} Fe ₂ O ₄	Co ²⁺ _{0.2} Cu ²⁺ _{0.18} Zn ²⁺ _{0.1} Fe ³⁺ _{0.52}	Co ²⁺ _{0.3} Cu ²⁺ _{0.22} Fe ³⁺ _{1.48}
Co _{0.5} Cu _{0.3} Zn _{0.2} Fe ₂ O ₄	Co ²⁺ _{0.08} Cu ²⁺ _{0.12} Zn ²⁺ _{0.2} Fe ³⁺ _{0.6}	Co ²⁺ _{0.42} Cu ²⁺ _{0.18} Fe ³⁺ _{1.4}
Co _{0.5} Cu _{0.2} Zn _{0.3} Fe ₂ O ₄	Cu ²⁺ _{0.1} Zn ²⁺ _{0.3} Fe ³⁺ _{0.6}	Co ²⁺ _{0.5} Cu ²⁺ _{0.1} Fe ³⁺ _{1.4}
Co _{0.5} Cu _{0.1} Zn _{0.4} Fe ₂ O ₄	Cu ²⁺ _{0.05} Zn ²⁺ _{0.4} Fe ³⁺ _{0.55}	Co ²⁺ _{0.5} Cu ²⁺ _{0.05} Fe ³⁺ _{1.45}
Co _{0.5} Zn _{0.5} Fe ₂ O ₄	Zn ²⁺ _{0.5} Fe ³⁺ _{0.5}	Co ²⁺ _{0.5} Fe ³⁺ _{1.5}

where λ is the wavelength of the electron wave, L is the camera wavelength, and R is the radius of the diffraction ring. The average grain size of $x=0.0$ is 0.341 μm .

3.4 FTIR studies

The sintered powder of the samples was used for the FTIR study between 380 and 800 cm^{-1} the pattern of which the two main absorption bands in between 4000 and 600 cm^{-1} wavenumber range shown in Fig. 8. The vibration of the Me–O bonds at the B site with a lower frequency band (ν_2) is around 400 cm^{-1} , and that at the A site with a higher frequency band (ν_1) is around 600 cm^{-1} . The difference in the two wave numbers is due to the different bond lengths (2.03 Å and 1.92 Å) at the two sites B and A, respectively [29]. Due to the Jahn–Teller phenomenon, the local deformations in the Fe²⁺ ion bonds take place.

The force constants at the two sites A and B are, respectively, given by

$$K_t = 7.62 \times M_1 \times \nu_1 \times 10^{-3} \text{ dynes/cm},$$

$$K_o = 10.62 \times M_2 \times \nu_2 \times 10^{-3} \text{ dynes/cm},$$

where the respective molecular weights are M_1 and M_2 in the B and A sites.

Variations of the tetrahedral and octahedral force constants of the synthesized samples are shown in Fig. 9. Two prominent absorption bands (ν_1 and ν_2) around 400 and 600 cm^{-1} , respectively, are observed. These spectra represent the characteristic features of the ferros spinels, and the bands are attributed to the stretching vibration due to interactions between the oxygen atom and the cations in the tetrahedral and octahedral sites, respectively. The difference between ν_1 and ν_2 is due to the changes in bond length (Fe–O) at the octahedral and tetrahedral sites. The FTIR spectroscopic results are summarized in Table 3. It is clear that the bond lengths are inversely related to force constants. From the table, it is clear that both bands are perturbed with the incorporation of Zn ions in the CoCu matrix. Significant changes were observed in the ν_1 band (corresponding to the tetrahedral site) and also a prominent perturbation was observed in the ν_2 band (corresponding to the octahedral site). The frequency of the band was observed to change

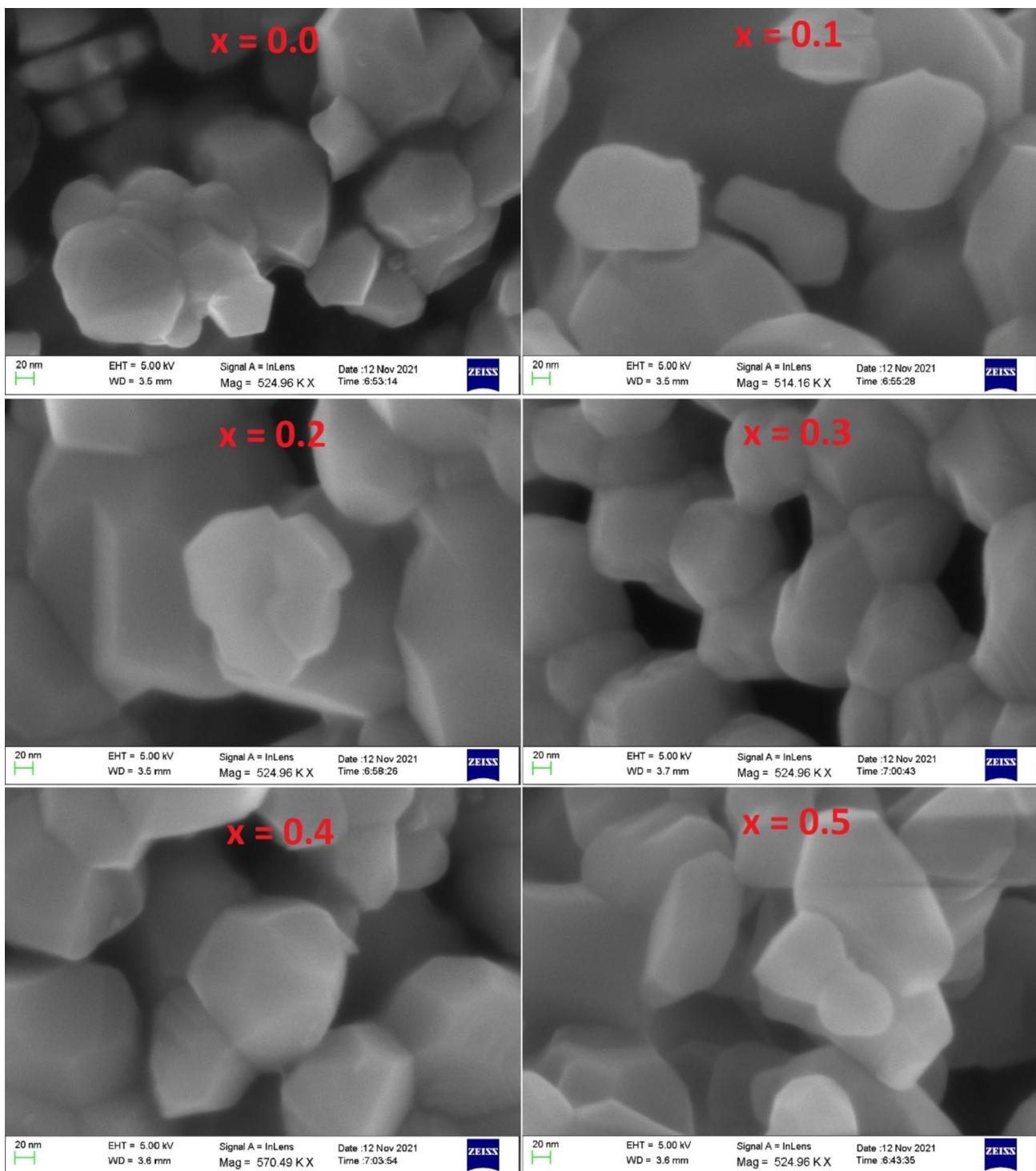


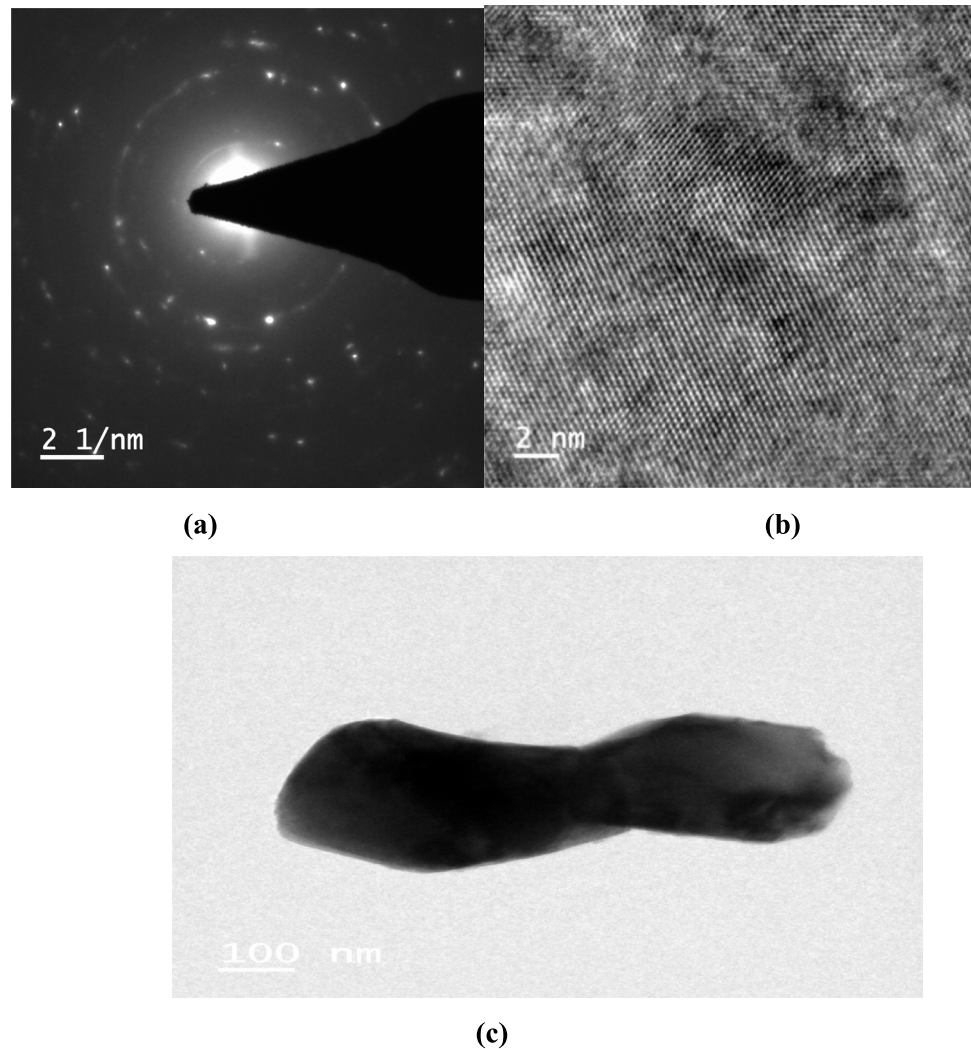
Fig. 5 FESEM of the CoCuZn nanoferrite system

from low frequency to higher frequency with progressive doping. The behavior is attributed to stretching of the Fe–O bonds on substitution of Zn ions.

On increasing Zn substitution, the characteristic band ν_1 shifts to the lower-frequency region, i.e., from

580 to 576 cm^{-1} due to the stretching vibration of the $\text{Fe}^{3+}\text{--O}^{2-}$ bonds on the substitution of Zn ions, while at the same time ν_2 shifts to the higher-frequency region as investigated, i.e., from 412 to 435 cm^{-1} with Zn addition. A similar result was observed with the incorporation of

Fig. 6 a–c HRTEM micrographs of the CoCuZn ($x=0.0$) nanoferrite system



In $\text{Ni}_{0.5}\text{Cu}_{0.25}\text{Zn}_{0.25}\text{Fe}_{2-x}\text{In}_x\text{O}_4$ [30]. Stretching vibrational bands that were found using FTIR data are shown in Table 3, which depicts that both the vibrational bands are disturbed with the addition of Zn ions.

The increase in the force constant for the tetrahedral complex with the incorporation of Zn²⁺ ions suggests a strengthening of the inter-atomic bonding between Me and O and is subsequently reflected in the distances between the cations and anion. With an increase in Zn²⁺ concentration, the wavenumber of the octahedral absorption band gradually increases. The M–O distance in two different sites determines the position of the tetrahedral and octahedral bands. As a result, the wavenumber values at the two sites are different. The fundamental frequency rises as the site radius or bond length decreases. All these make the frequency center shift toward higher frequencies showing the existence of Zn²⁺ ions in the B site. For the concentration $x=0.2$, the site radius and bond length increased due to Zn²⁺ replacement by Cu²⁺. As the concentration becomes higher, the transfer of ions takes place from one site to another, causing

a decrease in site radius again [31]. The FTIR curves show that the higher frequency at the concentration $x=0.2$ causes many absorptions.

3.5 VSM analysis

Figure 10 depicts the hysteresis loops of $\text{Co}_{0.5}\text{Cu}_{0.5-x}\text{Zn}_x\text{Fe}_2\text{O}_4$ ($x=0.0, 0.1, 0.2, 0.3, 0.4$ and 0.5) ferrites at room temperature. This plot is used to determine the saturation magnetization (M_s), coercivity (H_c), and remanent magnetizations (M_r), which are all provided in Table 4. In comparison to previously reported values [32], the saturation magnetization of pure $\text{Co}_{0.5}\text{Cu}_{0.5}\text{Fe}_2\text{O}_4$ is much lower in the present work. Magnetization versus applied magnetic field (M – H) measurements were carried out under room temperature. In each hysteresis loop cycle, the magnetization data were recorded while the applied field was varied between 10 and 10KOe. The saturation magnetization values were found from the linear extrapolation of the M versus $1/H$ curves for the limit when $1/H$ approaches zero. The magnetization

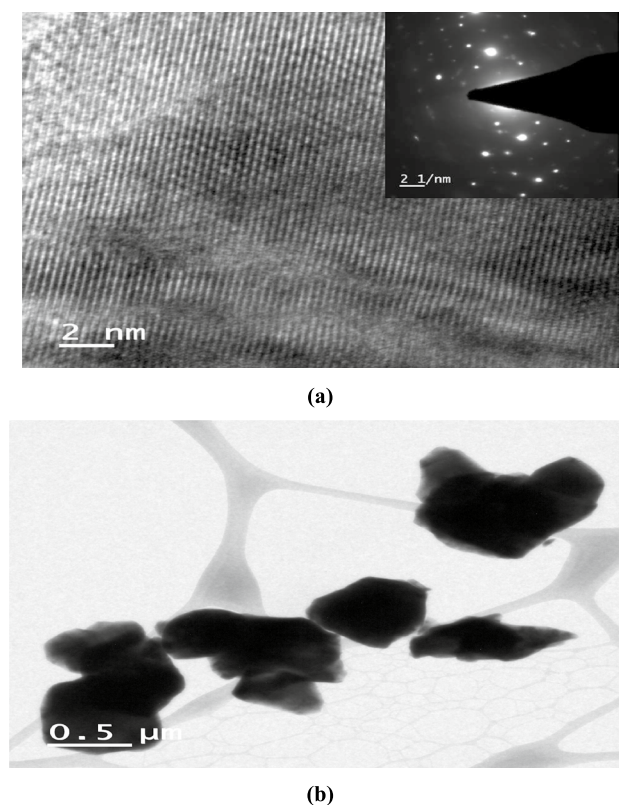


Fig. 7 a, b HRTEM micrographs of the CoCuZn ($x=0.1$) nanoferrite system

depends on the cation distribution among A and B locations. The saturation magnetization (M_s) increases from $x=0.0$ to $x=0.1$ and then decreases to $x=0.2$ to $x=0.5$ for an increase in the Zn^{2+} content as shown in Fig. 11. The redistribution of cations is the primary cause of the observed variation in saturation magnetization. The observed non-linear variation in magnetization is due to the Zn^{2+} ions distributed in both the A (in place of Cu^{2+} ions) and B sites at the same time. The maximum enhancement of magnetic properties for the replacement of the non-magnetic Zn cations in place of Cu can be obtained for $x=0.1$ substitutions. The decrease in (M_s) values with the higher concentrations of non-magnetic Zn^{2+} ions can be recognized to the effect on saturation magnetization which is clarified on the basis of the spin canting effect [33]. Other reason for reduction of saturation magnetization is due to the substitution of lower magnetic moment Zn^{2+} ions ($0\mu B$) that replaced the Cu^{2+} ions ($1\mu B$). Each sublattice is spontaneously magnetized and aligned in the opposite direction to the others in ferromagnetic materials [34].

Thus, the net magnetic moment is given by $|M| = |M_B - M_A|$, where M_A and M_B are the magnetic moment at the A and B sites, respectively. Table 4 shows that the distribution of Zn^{2+} ions in A and B is equal. The magnetization

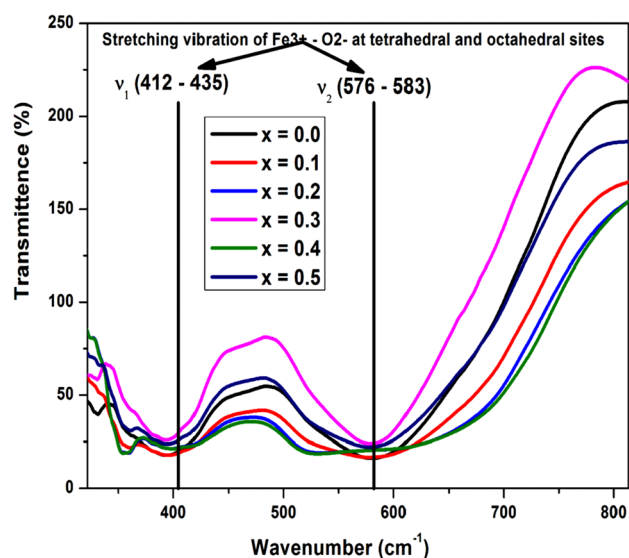


Fig. 8 Absorption spectra of the CoCuZn nanoferrite system

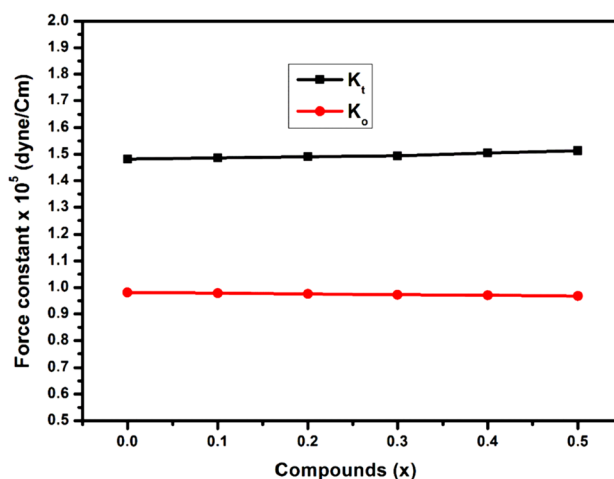


Fig. 9 Force constants of the CoCuZn nanoferrite system

(M) decreases as the Zn^{2+} concentrations increase, because the magnetization of the A sublattice increases and that of the B sublattice decreases. Additionally, the migration of a higher concentration of Co^{2+} ions into A sites, which forces Fe^{3+} ions into octahedral sites and increases M_s value, is the cause of the increase in magnetization for $x=0.1$. For reduced remanence to be zero, coercivity is the minimum reverse magnetic field strength required.

The theoretical ($\mu_{Bth.}$) and experimental ($\mu_{Bobs.}$) Bohr magnetons were calculated and the variation with respect to Zn composition is represented in Table 4. The theoretically calculated values depend on the cation distribution over the A and B sites, i.e., $[Zn^{2+x}Fe^{3+}]^A [Co^{2+}_{0.5}Cu^{2+x}Zn^{2+}_{1-x}Fe^{3+}]^B O_4$. The observed magneton

Table 3 FTIR parameters of the CoCuZn nanoferrite system

Compounds (x)	Tetrahedral ν_1 (cm ⁻¹)	Octahedral ν_2 (cm ⁻¹)	$K_t \times 10^5$ dyne/cm	$K_o \times 10^5$ dyne/cm
Co _{0.5} Cu _{0.5} Fe ₂ O ₄	580	412	1.482	0.981
Co _{0.5} Cu _{0.4} Zn _{0.1} Fe ₂ O ₄	579	413	1.486	0.979
Co _{0.5} Cu _{0.3} Zn _{0.2} Fe ₂ O ₄	583	415	1.491	0.976
Co _{0.5} Cu _{0.2} Zn _{0.3} Fe ₂ O ₄	580	419	1.494	0.973
Co _{0.5} Cu _{0.1} Zn _{0.4} Fe ₂ O ₄	578	422	1.505	0.971
Co _{0.5} Zn _{0.5} Fe ₂ O ₄	576	435	1.513	0.968

number (η_{Bobs}) was calculated by using the values of saturation magnetization and using the formula [35]

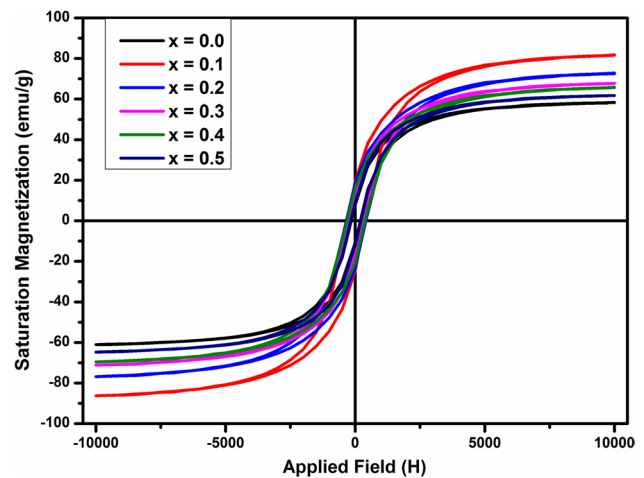
$$\eta_B = \frac{MW \times Ms}{5585},$$

where Ms is the specific saturation magnetization (emu/g), η_B is the magnetic moment (Bohr magneton, B.M.), and MW is the composition's molecular weight.

The magneton number increases with Zn²⁺ content 'x' increases up to $x=0.1$ and then decreases up to $x=0.2$ and again increasing starts from at $x=0.3$. The enhancement in the magneton number is attributed to the fact that due to the predominant inter-sublattice A–B super-exchange interaction, the net magnetic moment per formula is increased which causes the increase in the magneton number of the system [36, 37]. It is found from Table 4 that the calculated experimental values (μ_{Bobs}) are not in good agreement with the observed values of (μ_{Bobs}), suggesting that significant canting exists at octahedral B sites which can be explained on the basis of three sublattice models suggested by Yafet–Kittel [38].

The hysteresis curves in Fig. 11 reveal that the nanoferrite samples exhibited low coercivity, indicating that they are part of the soft ferrites family. Coercivity is influenced by factors such as particle size, porosity, secondary phases, magnetocrystalline anisotropy, and lattice defects [39]. The variation of coercivity (H_c) in this study varies from that of Ms and Mr. From Table 4, it can be observed that H_c increases initially and becomes a maximum of $x=0.3$, and then falls from $x=0.4$ to $x=0.5$. This study's magnetocrystalline anisotropy of octahedral Zn²⁺ ions increases the

coercive field. Additionally, the anisotropy of the B sites is decreased by the movement of Co from B to A sites, which lowers H_c . The coercivity varies inversely with grain size, as is well known. Greater numbers of domain walls would be seen in samples with larger grain sizes. The domain wall movement needs less energy than that for the domain rotation [40]. Therefore, it is expected that samples with larger grain sizes will have low coercivity values. The remnant ratio gives the easiness for the reorientation of the magnetic material after the removal of the magnetic field. The remnant ratio of the samples was found between 0.19 and 0.8. The materials' isotropic nature is indicated by the low value of R.

**Fig. 10** Hysteresis curves of the CoCuZn nanoferrite system**Table 4** Magnetic parameters of the CoCuZn nanoferrite system

Compounds (x)	M_s (emu/g)	M_r (emu/g)	H_c (Oe)	μ_B (obs.)	μ_B (th.)	$K_1 \times 10^4$ (erg/cc)	$R = M_r/M_s$
Co _{0.5} Cu _{0.5} Fe ₂ O ₄	60.97	11.8	112	2.1	5.3	0.8	0.19
Co _{0.5} Cu _{0.4} Zn _{0.1} Fe ₂ O ₄	86.35	11.7	125	2.45	5.2	0.9	0.14
Co _{0.5} Cu _{0.3} Zn _{0.2} Fe ₂ O ₄	76.93	11.9	305	1.8	5.1	1.3	0.15
Co _{0.5} Cu _{0.2} Zn _{0.3} Fe ₂ O ₄	71.20	10.5	415	1.9	5.6	1.8	0.16
Co _{0.5} Cu _{0.1} Zn _{0.4} Fe ₂ O ₄	69.51	6.5	201	3.1	6.1	1.4	0.09
Co _{0.5} Zn _{0.5} Fe ₂ O ₄	64.67	5.3	182	4.1	6.6	1.7	0.08

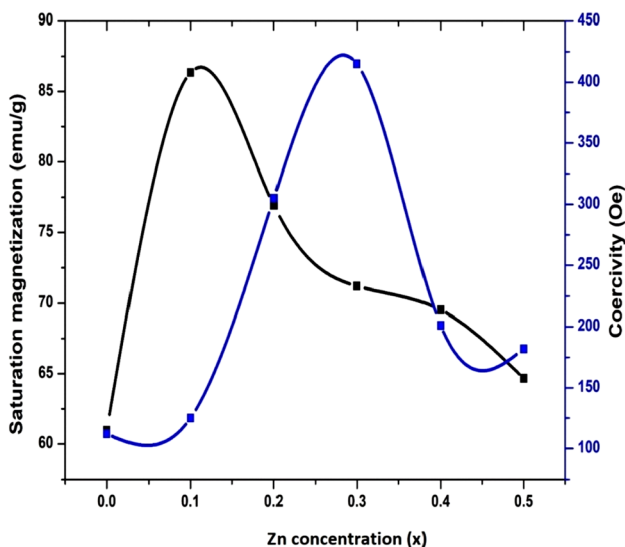


Fig. 11 Saturation magnetic vs. coercivity of the CoCuZn nanoferrite system

3.6 Permeability studies

The frequency dependency of the magnetic initial permeability μ_i at 300 K and the change in μ_i with Zn^{2+} content for our samples are shown in Fig. 12 and Fig. 13, respectively. The μ_i toroid-shaped samples were calculated using the following relation.

There are a larger number of domain walls in larger grains whose displacement gives rise to the initial permeability [41]:

$$\mu_{iw} = \frac{3\mu_0 Ms^2 D}{16\gamma_w}$$

where μ_{iw} is the initial permeability due to domain wall rotation, μ_0 is the free space permeability, Ms is the saturation magnetization, D is the average grain size, and γ_w is the domain wall energy.

It is observed that μ_i is high at low frequency and decreases gradually with increasing frequency for all samples. This behavior may be related to the domain wall motion effect. The μ_i becomes constant from about 15–50 MHz with a further increase in frequency indicating high-frequency stability of all samples. Similar behaviors have also been reported in the literature [42]. This suggests that all the synthesized samples can be used in high-frequency devices. It is also found that samples with $x=0.1-0.2$ provide larger μ_i compared to the synthesized sample over the measured frequency range. However, μ_i values are lower for samples with $x=0.3-0.5$ than for the parent compound.

As observed in Figure, μ_i first decreases sharply and then increases with a further increase in Zn^{2+} content from

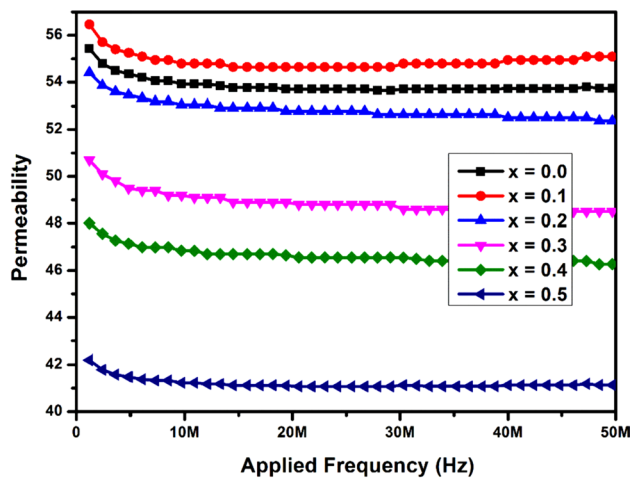


Fig. 12 Initial permeability vs frequency of the CoCuZn nanoferrite system

$x=0.0-0.5$. The maximum μ_i is obtained for $x=0.5$ in the synthesized samples. In this study, we identified that grain size and μ_i showed similar behavior with the variation of Zn^{2+} content, confirming the existence of a correlation between grain sizes and μ_i , which is in good agreement with the μ_i results reported [43–45]. As reported, ferrite materials having larger grain sizes exhibited an enhanced μ_i [46].

3.7 DC resistivity study

The composition and method of preparation affect greatly the ferrite’s properties. The fluctuation in DC electrical resistivity as a function of the sample nanoferrites is shown in Fig. 14. Zn^{2+} concentration has a noticeable influence on DC resistivity. The two-probe method was used for the

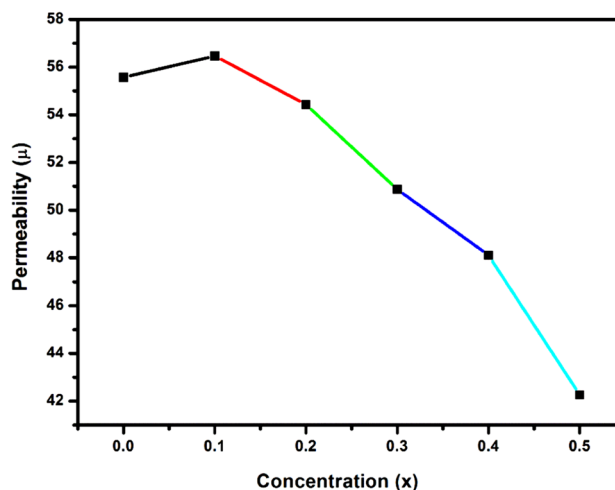


Fig. 13 Frequency dependence of the initial permeability of the CoCuZn nanoferrite system

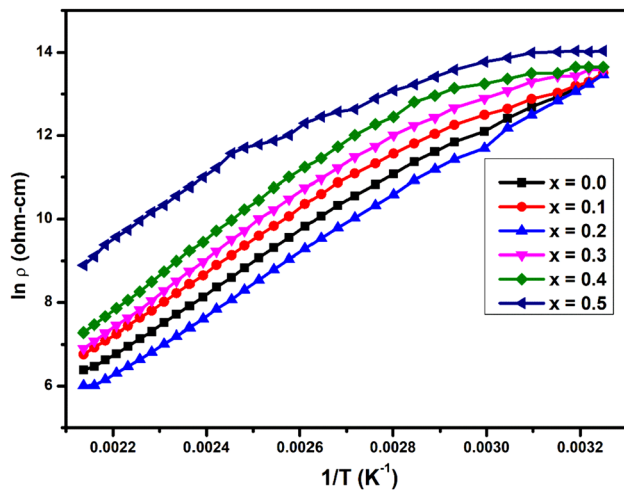


Fig. 14 Temperature dependence of DC electrical resistivity of the CoCuZn nanoferrite system

measurement of the DC resistivity of the synthesized samples. The DC resistivity increases with the increase of Zn²⁺ concentration. The ferrous ions are formed at the B site with the loss of zinc during sintering at higher temperatures [47]. The electrical conductivity varies according to the Verwey de Boer hopping mechanism [48], in which the electrons jump from one ion to another ion of the same element at different valence states [49]. The occupancy of these ions in two interstitial sites depends on their ionic radii and crystal field stabilization energy.

The larger divalent element occupies the B site and the smaller trivalent element occupies the A site. The distances between cations at B sites are closer together than those at A sites. This indicates that the hopping of holes and electrons between ions at the B–B sites is more prevalent than at the A–A sites. Because the overlap of orbitals is larger and the chance of hopping is higher, the distance between the cations is lower. When ferrite samples are sintered in an environment of air, zinc volatilization from the samples takes place at significantly higher temperatures [50]. Zn²⁺ evaporation from the substance causes cation vacancies and unsaturated O₂ ions, which alter the substance's stoichiometry [51]. To maintain the charge balance in the lattice, the extra electrons on the saturated oxygen ion then connect with nearby ferric (Fe³⁺) ions, resulting in the creation of ferrous (Fe²⁺) ions in the ferrite. Therefore, the overall resistivity of ferrite materials is controlled by the ratio of Fe²⁺/Fe³⁺ on B sites.

The concentration of Fe³⁺ ions at both B and A sites were altered simultaneously by the statistical distribution of Zn²⁺ ions proposed between the two sites. While Fe³⁺ ions occupy both A and B sites, Zn²⁺ ions prefer to occupy A sites, while Co²⁺ ions prefer to occupy B sites. Upon Zn²⁺ substitution, some Fe³⁺ ions moved from the B site to the A site, thereby

diluting the exchange between the Fe²⁺ and Fe³⁺ electron exchange.

Higher resistivity values in the current system reflect very low Fe²⁺ ion formation, which suggests minimal Cu²⁺ loss during sintering. Higher concentrations of Zn²⁺ will occupy A sites, moving Fe³⁺ ions from A to B sites in the process. The number of Fe²⁺ and Fe³⁺ pairs will increase due to the increase in Fe³⁺ ions at B sites, which increases the probability of hopping. As a result, the addition of Zn²⁺ caused the resistivity to decrease. In general, the density, porosity, particle size, and chemical composition of the sample all affect the resistivity of ferrites. According to studies, these ferrites' conductivity results from electron hopping between Fe ions in various valence states (Fe²⁺ and Fe³⁺) that are present on equivalent lattice sites. Along with the aforementioned effects, the decrease in porosity also has an impact on resistivity, since pores act as a source of scattering centers. The important reduction in the BO₆ bond length of the octahedral site (B) brought on by the migration of Co²⁺ ions into the A-site may also have contributed to the observed DC resistivity increases $x = 0.5$ and then decreases with Zn²⁺ concentration decreased. In addition, compared to other compositions in the samples, more Zn²⁺ ions enter the B site. Therefore, a decrease in the distances between the cations at B sites and an increase in the chance of charge hopping may be related to a decrease in resistivity. Moreover, the occurrence of a localized stage in the forbidden energy gap, which results from lattice defects, may also contribute to the compositions' decreased resistivity. These states effectively reduce the energy barriers preventing electron transport [52].

The above arguments lead one to the conclusion that the microstructure (porosity, grain size), density of ferrous ions, and resistivity of ferrites are all determined by these factors. All of the samples' DC electrical resistivity displays semiconductor-like behavior, with all of the samples' resistivities decreasing with increase in temperature. In ferrites, this behavior as temperature increases is caused by the thermal mobility of charge carriers rather than by an increase in charge carriers as temperature increases, since electron hopping between octahedral sites only requires a relatively small amount of energy at higher temperatures [53].

According to the Arrhenius relation [54]:

$$\rho = \rho_0 e^{-\left(\frac{\Delta E}{KT}\right)},$$

where ΔE is the activation energy and K is the Boltzmann constant.

The inset in Fig. 15 shows the activation energy vs. Zn²⁺ concentration. The observed differences in the

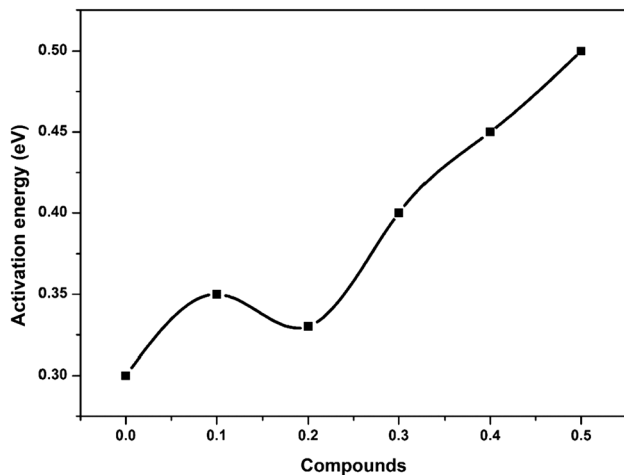


Fig. 15 Comparing the composition and activation energy of the CoCuZn nanoferrite system

samples' resistivity values are consistent with the reported variation in activation energies. Since the distance between octahedral sites is smaller than that between tetrahedral sites, electron hopping occurs between octahedral sites in spinel ferrites. The activation energies needed for the electron hopping between Fe^{2+} and Fe^{3+} at the B sites have been reported to be around 0.5 eV [55]. For Zn substituted Co–Cu ferrite, the decrease in lattice constant means a decrease in their ionic radii in A and B sites. As a result, hopping charge carriers see a decrease in barrier height.

Here, the grain size also reduces when Zn^{2+} concentration increases. Therefore, it is reasonable to assume that the activation energy will increase with Zn^{2+} substitution. In contrast to the explanation above, it has been found that the activation energies in the system increase with Zn^{2+} substitution up to $x=0.5$. On the other side, the activation energy is also influenced by density, porosity, and particle size. The pores reduce the charge carriers' ability to move between sites, increasing the resistivity [56, 57].

4 Conclusion

The samples were successfully synthesized with the sol–gel route and found to be single-phase nanocrystalline. The increase in the lattice constant is evidence that Zn^{2+} ions' solubility in the spinel lattice indicates the increasing lattice constant. The cation distribution in the prepared ferrite is very complex. The FESEM images give the grain size of each sample. The FTIR spectra confirm the distribution of Zn^{2+} ions in the octahedral position. DC electrical resistivity and activation energies were calculated. The substitution of Zn^{2+} ions has an impact on density, particle size, and grain size. $\text{Co}_{0.5}\text{Cu}_{0.4}\text{Zn}_{0.1}\text{Fe}_2\text{O}_4$ has a higher saturation

magnetization than that indicated by magnetic measurements. The saturation magnetization is decreased due to spin canting between the sites, but is negligible. Higher saturation magnetization and lower coercivity make these materials applicable in recording media.

Acknowledgements This research received no external funding.

Data availability statement Data is available on request to the corresponding author.

Declarations

Conflict of interest There are no conflicts to declare.

References

1. S. Yonatan Mulushoa, C.V. Kumari, R. Vemuri, K. Ephraim Babu, B.S.N. Murthy, K. Suribabu, Y. Ramakrishna, N. Murali, *Physica B Condens* **572**, 139–147 (2019)
2. K. Manju, S. Thankachan, D.S. Nair, E.K. Aswathy, A. Babu, A. Thomas, B.K.T. Krishna, *J. Adv. Ceram.* **4**, 199–205 (2015)
3. A. Ramakrishna, N. Murali, T. Wegayehu Mammo, K. Samatha, V. Veeraiah, *Phys. B Condens. Matter* **534**, 134–140 (2018)
4. R.C. Kambale, P.A. Shaikh, C.H. Bhosale, K.Y. Rajpure, Y.D. Kolekar, *Smart Mater. Struct.* **18**(11), 115028 (2009)
5. G. Raju, N. Murali, M.S.N.A. Prasad, B. Suresh, D. Apparao Babu, M. Gnana Kiran, A. Ramakrishna, M. Tulu Wegayehu, B. Kishore Babu, *Mater. Sci. Energy Technol.* **2**, 78–82 (2019)
6. F. Ansari, A. Sobhani, M. Salavati-Niasari, *J. Colloid Interface Sci.* **514**, 723–732 (2018)
7. K. Sakthipandi, B. Ganesh Babu, G. Rajkumar, A. Hossian, M. Srinidhi Raghavan, M. Rajesh Kumar, *Physica B Condens* **645**, 414280 (2022)
8. K.J. Standley, *Oxide magnetic materials* (Oxford University Press, USA, 1972)
9. G. Fagherazzi, F. Garbassi, *J. Appl. Crystallogr.* **5**(1), 18–23 (1972)
10. V. Pissurlekar, *J. J. Sci. Res.* **4**, 453–456 (2015)
11. N. Sanpo, J. Wang, C.C. Berndt, *J. Nano Res.* **25**, 110–121 (2013)
12. K.N. Hari, G. Aravind, D. Ravinder, T. Somaiah, B. Ravinder Reddy, *Int. J. Eng. Res. Appl.* **4**, 137–141 (2014)
13. A. Ramakrishna, N. Murali, S.J. Margarette, T.W. Mammo, N.K. Joythi, B. Sailaja, C.C. Sailajaumari, K. Samatha, V. Veeraiah, *Adv. Powder Technol.* **29**, 2601–2607 (2018)
14. M.S. Khandekar, R.C. Kambale, J.Y. Patil, Y.D. Kolekar, S.S. Suryavanshi, *J. Alloy. Compd.* **509**(5), 1861–1865 (2011)
15. S.S. Abbas, I.H. Gul, S. Ameer, M. Anees, *Electron. Mater. Lett.* **11**(1), 100–108 (2015)
16. K. Muhammad Azhar, M. Islam ul, M. AsifIqbal, M. Ahmad, M.F. Din, G. Murtaza, I. Ahmad, M.F. Warsi, *Ceram. Int* **40**, 3571–3577 (2014)
17. H.R. Daruvuri, K. Chandu, N. Murali, D. Parajuli, M.P. Dasari, *Inorg. Chem. Commun* **143**, 109794 (2022)
18. T. Dippong, E.A. Levei, O. Cadar, Formation, structure and magnetic properties of $\text{MFe}_2\text{O}_4@ \text{SiO}_2$ ($\text{M} = \text{Co}, \text{Mn}, \text{Zn}, \text{Ni}, \text{Cu}$) *Nanocompos. Mater* **2021**(14), 1139 (2021)
19. M.S. Yonatan, C.V. Kumari, V. Raghavendra, K. Ephraim Babu, B.S.N. Murthy, K. Suribabu, Y. Ramakrishna, N. Murali, *Phys. B Condens. Matter* **572**, 139–147 (2019)

20. P.N. Vasambekar, C.B. Kolekar, A.S. Vaingankar, *Mater. Chem. Phys.* **60**(3), 282–285 (1999)
21. A.M.A. Henaish, O.M. Hemeda, B.I. Salem, F.S. El-Sbakhy, T. Khalass, *J. Phys. Conf. Series* **1253**, 012025 (2019)
22. L.G. Van Uitert, *J. Chem. Phys.* **24**(2), 306–310 (1956)
23. M.A. Ali, M.N.I. Khan, F.U.Z. Chowdhury, M.M. Hossain, M.Z. Rahaman, S.M. Hoque, M.A. Matin, M.M. Uddin, *Results Phys.* **14**, 102517 (2019)
24. P. Himakar, K. Jayadev, D. Parajuli, N. Murali, P. Taddesse, S. Yonatan Mulushoa, T. Wegayehu Mammo, B. Kishore Babu, V. Veeraiah, K. Samatha, *Appl. Phys. A* **127**, 1–10 (2021)
25. N. Murali, S.J. Margarete, G. Pavan Kumar, B. Sailaja, S. Yonatan Mulushoa, P. Himakar, B. Kishore Babu, V. Veeraiah, *Phys. B Condens. Matter* **522**, 1–6 (2017)
26. A. Ramakrishna, N. Murali, S.J. Margarete, K. Samatha, V. Veeraiah, *Physica B* **530**, 251–257 (2018)
27. K. Chandramouli, P. AnanthaRao, B. Suryanarayana, V. Raghavendra, S.J. Mercy, D. Parajuli, P. Taddesse, S. Yonatan Mulushoa, T. WegayehuMammo, N. Murali, *J. Mater. Sci. Mater. Electron.* **32**, 15754–15762 (2021)
28. K.M. Batoo, M.S. Ansari, Low temperature-fired Ni-Cu-Zn ferrite nanoparticles through auto-combustion method for multilayer chip inductor applications. *Nanoscale Res. Lett.* **7**, 112 (2012)
29. M. Hashim Alimuddin, S.E. Shirsath, S. Kumar, R. Kumar, A.S. Roy, J. Shah, R.K. Kotnala, Preparation and characterization chemistry of nano-crystalline Ni–Cu–Zn ferrite. *J. Alloy. Compd.* **549**, 348–357 (2013)
30. M.T. Wegayehu, N. Murali, Y. Mulushoa Sileshi, T. Arunamani, *Phys. B Condensed Matter* **531**, 164–170 (2018)
31. B. Madhavilatha, D. Parajuli, K. Jayadev, C. Komali, N. Murali, V. Veeraiah, K. Samatha, *Biointerface Res. Appl. Chem.* **12**, 1899–1906 (2021)
32. K. Ramanjaneyulu, B. Suryanarayana, V. Raghavendra, N. Murali, D. Parajuli, K. Chandramouli, *Solid State Technol.* **64**, 7192–7200 (2021)
33. A.M. ElNahrawy, A.M. Mansour, H.A. ElAttar, E.M.M. Sakr, A.A. Soliman, A.B.A. Hammad, Impact of Mn substitution on structural, optical, and magnetic properties evolution of sodium-cobalt ferrite for opto-magnetic applications. *J Mater Sci: Mater Electron* **31**, 6224–6232 (2020)
34. K. Chandramouli, B. Suryanarayana, P.V.S.K. Phanidharvarma, V. Raghavendra, K.A. Emmanuel, P. Taddesse, N. Murali, T.W. Mammo, D. Parajuli, *Results in Physics* **24**, 104117 (2021)
35. R. Köferstein, T. Walther, D. Hesse, S.G. Ebbinghaus, *J. Solid State Chem.* **213**(2014), 57–64 (2014)
36. J. Xia, X. Wu, Y. Huang, W. Wu, J. Liang, Q. Li, *J. Mater. Sci. Mater. Electron.* **30**(12), 11682–11693 (2019)
37. C. Nayek, K. Manna, G. Bhattacharjee, P. Murugavel, I. Obaidat, *Magnetochemistry* **3**(2), 19 (2017)
38. Y. Yafet, C. Kittel, *Phys. Rev.* **90**, 295 (1952)
39. E. Shirsath Sagar, R.H. Kadam, M.L. Mane, A. Ghasemi, Y. Yasukawa, X. Liu, A. Morisako, *J. Alloy. Compd* **575**, 145–151 (2013)
40. S.V. Bhandare, R. Kumar, A.V. Anupama, M. Mishra, R. Vijaya Kumar, V.M. Jali, B. Sahoo, *Mater. Chem. Phys.* **251**, 123081 (2020)
41. R.H. Kadam, A.P. Birajdar, T.A. Suresh, E.S. Sagar, *J. Magn Magn Mater* **327**, 167–171 (2013)
42. D.R. Mane, D.D. Birajdar, P. Swati, E.S. Sagar, R.H. Kadam, *J. Sol-Gel Sci. Technol.* **58**, 70–79 (2011)
43. A.M. Mohammad, M.M. Mohammed, L.A. Hussein, *Dig. J. Nanomater. Biostruct.* **15**(1), 231–241 (2020)
44. K.M. Somnath, E.H. Batoo, S.F. Raslan, A. Induharma, G. Kumar, *J. Mater Sci* **31**, 7880–7888 (2020)
45. S. Anjana, K. Mujasam Batoo, E.H. Raslan, G. Kumar, *J. Mater. Sci. Mater. Electron.* **31**, 16959–16967 (2020)
46. K. Gagan, R.K. Kotnala, J. Shah, V. Kumar, A. Kumar, P. Dhiman, M. Singh, *Phys. Chem. Chem. Phys.* **19**, 16669–16680 (2017)
47. G.V. Priya, N. Murali, M.K. Raju, B. Krishan, D. Parajuli, P. Choppara, B.C. Sekhar, R. Verma, K.M. Batoo, P.V. Narayana, *Appl. Phys. A* **128**, 1–8 (2022)
48. L.M. Thorat, J.Y. Patil, D.Y. Nadargi, U.R. Ghodake, R.C. Kambale, S.S. Suryavanshi, *J. Adv. Ceram.* **7**, 207–217 (2018)
49. P. Monisha, P. Priyadharshini, S.S. Gomathi, K. Pushpanathan, *J. Alloy. Compd.* **856**, 157447 (2021)
50. J.C.R. Araújo, S. Araujo-Barbosa, A.L.R. Souza, C.A.M. Iglesias, J. Xavier, P.B. Souza, C.C. Plá Cid et al., *J. Phys. Chem. Solids* **154**, 110051 (2021)
51. C. Komali, N. Murali, D. Parajuli, A. Ramakrishna, Y. Ramakrishna, K. Chandramouli, *Indian J. Sci. Technol.* **14**, 2309–2316 (2021)
52. M. Madhu, A.V. Rao, D. Parajuli, S.Y. Mulushoa, N. Murali, *Inorg. Chem. Commun.* **143**, 109818 (2022)
53. M.P. Reddy, X. Zhou, A. Yann, S. Du, Q. Huang, A.M.A. Mohamed, *Superlattices Microstruct.* **81**, 233–242 (2015)
54. M. Islam, M. Jhahan, M.T. Khatun, M.N.I. Khan, M.J. Rahman, A. Al-Momin, M.M. Alam, *J. Mater. Sci.: Mater. Electron.* **32**, 26173–26180 (2021)
55. R. Yang, X. Yu, H. Li, C. Wang, C. Wu, W. Zhang, W. Guo, *J. Alloy. Compd.* **851**, 156907 (2021)
56. B. R. Vergis, N. Kottam, R. H. Krishna, G. N. Anil Kumar, *Materials Today Proceedings*, (2021)
57. M. Kaiser, A. Hashhash, H.E. Hassan, *Appl. Phys. A* **127**, 1–13 (2021)

Publisher's Note Springer Nature remains neutral with regard to jurisdictional claims in published maps and institutional affiliations.

Springer Nature or its licensor (e.g. a society or other partner) holds exclusive rights to this article under a publishing agreement with the author(s) or other rightsholder(s); author self-archiving of the accepted manuscript version of this article is solely governed by the terms of such publishing agreement and applicable law.